Design of Frequency-Adaptive Flux Observer in PMSM Drives Robust to Discretization Error

Jiwon Yoo, *Student Member*, *IEEE*, Hyeon-Sik Kim, *Member*, *IEEE*, and Seung-Ki Sul, *Fellow*, *IEEE*

***Abstract*—This paper analyzes the effect of discretization in the frequency-adaptive flux observer (FAO). Although FAO has structural simplicity and ease of implementation, the discrete-time FAO has phase and gain errors in fundamental flux estimation. As a result, the estimated flux might be erroneous, especially in the high-speed region. For accurate flux estimation, this paper analyzes how the voltage synthesis in the pulse-width-modulation (PWM) affects the stator flux. Through the analysis, the backward Euler method is selected for the primitive stator flux estimation. To mitigate the FAO's discretization error, the proposed FAO utilizes the integrators constructed at the rotor reference frame. Since the discretization error comes from the approximation error of the continuous-time integrator at the operating frequency, the proposed FAO conducts the fundamental flux extraction at the rotor reference frame, where the operating frequency components are treated as a dc signal. Thanks to the coordinate transformation, the FAO can be discretized with no error while keeping the structure of double integrators. The proposed method is verified through the computer simulation and experimental test.**

***Index Terms*—Discretization, frequency-adaptive observer, flux observer, permanent-magnet synchronous motor.**

NOMENCLATURE

$(\,)^{\mathbf{s}}_{\mathbf{dq}} = (\,)^{s}_{d} + j(\,)^{s}_{q}$	*dq*-vector variable at the stationary reference frame.
$(\,)^{\mathbf{r}}_{\mathbf{dq}} = (\,)^{r}_{d} + j(\,)^{r}_{q}$	*dq*-vector variable at the rotor reference frame.
$(\hat{\,})$	Estimated value.
$(\,)^{*}$	Reference value.
$\mathbf{v}^{\mathbf{s}}_{\mathbf{dq}} = v^{s}_{d} + jv^{s}_{q}$	Stator voltage at the stationary reference frame.
$\mathbf{i}^{\mathbf{s}}_{\mathbf{dq}} = i^{s}_{d} + ji^{s}_{q}$	Stator current at the stationary reference frame.
$\boldsymbol{\lambda}^{\mathbf{s}}_{\mathbf{dq}} = \lambda^{s}_{d} + j\lambda^{s}_{q}$	Stator flux at the stationary reference frame.
θ_r	Electrical rotor angle.
ω_r	Electrical rotor speed.
T_s	Sampling period.

Manuscript received October 26, 2020; revised February 1, 2021 and March 8, 2021; accepted April 3, 2021. This work was supported in part by Seoul National University Electric Power Research Institute, in part by the Hyundai Motor Chung Mong-Koo Foundation, and in part by Brain Korea 21 Plus Project in 2020, granted financial resource from the Ministry of Trade, Industry, and Energy, Republic of Korea. *(Corresponding author: Jiwon Yoo.)*

Jiwon Yoo and Seung-Ki Sul are with the Department of Electrical and Computer Engineering, Seoul National University, Seoul, 08826, Korea (e-mail: jiwon.yoo@eepel.snu.ac.kr; sulsk@plaza.snu.ac.kr).

Hyeon-Sik Kim is with the Department of Electrical Engineering, Gachon University, Seongnam 13120, Korea (e-mail: hyeonsik@gachon.ac.kr).

I. INTRODUCTION

THE AC motor drives have become the standard in various industrial applications with induction motors (IMs) and permanent-magnet synchronous motors (PMSMs) in front. On the surface, the IMs and PMSMs have considerable differences in physical structure and control schemes. However, no matter what type of motor is, the stator flux information plays a crucial role in their control scheme. In IM drives, the flux observer is usually an essential part of conducting the field-oriented control (FOC) [1], [2]. Most sensorless PMSM drives also rely on the flux observer to estimate the rotor position [3], [4]. Besides, the stator flux information can be utilized in motor parameter estimation [5]-[7], temperature estimation [8], and loss-minimizing control [9]-[11].

Basically, the flux information can be obtained by the voltage model (VM) of the motor. In VM, the stator flux can be calculated by integrating the back electro-motive force (EMF). However, the pure integrator is not applicable due to its vulnerability to the dc offset error in the input signal, caused by its infinite gain at the zero-frequency [12], [13]. The simple solution for the dc drift problem would be applying a high pass filter in series to the pure integrator [14]. Although an integrator with a high pass filter (HPF) can be implemented with a simple low pass filter (LPF), the additional phase delay and magnitude distortion should be adequately compensated. In [1], [15], and [16], the phase and magnitude errors have been compensated with feedforward gain. In [16]-[20], the stator flux estimation at low-speed has been compensated with the current model (CM), which relies on the motor inductance information. CM-assisted flux observer can estimate the flux even at zero frequency, but it requires the inductance information, which may have an error caused by magnetic saturation or offline commissioning error.

Meanwhile, inverter non-linearity and spatial harmonics of the motor may prompt the low-order harmonics in flux estimation [20]-[22]. Since most applications require the fundamental flux information without harmonic components, various research works have studied the fundamental flux estimation in the presence of disturbances in input signals.

Since disturbance rejection is a mature research field in grid-synchronization, the various techniques in this field have been successfully transplanted in the flux estimation. In [23]-[25], the second-order generalized integrator-frequency locked loop (SOGI-FLL) based flux estimators have been proposed. SOGI-FLL effectively rejects the harmonic components and dc-offset using the double integrator. In [24], fifth and seventh order harmonic components were completely eliminated using a

multi-SOGI-FLL flux estimator.

Similar to SOGI-FLL, Park *et al.* [26] proposed a disturbance observer originated from the grid synchronization technique [27]. It estimates and removes the disturbance in the input voltage signal, keeping a simple structure based on the two cross-coupled integrators. Kim *et al.* [20] improved the harmonic-rejection performance of a disturbance observer combining with harmonic extractors.

Both SOGI-FLL and disturbance observer had been designed on the continuous-time domain, neglecting the effect of discretization in implementation. However, unlike the grid that has a relatively low frequency of 50/60 Hz, the stator flux of PMSM dynamically changes in a wide-range from dc to thousands of Hertz. The discretization error in flux observer would not only make an error in ripple components but also distort the fundamental flux waveform, which could adversely affect control performance. Therefore, to estimate the flux accurately for the wide speed range, the effect of discretization should be carefully considered in implementation [28], [29].

The implementation of a high-order frequency filter can be classified into two groups, approximation-based methods and direct discrete design. As analyzed in [29], the direct discrete design would provide satisfactory performance over the approximation-based methods. However, the direct discrete design requires complex analysis and computational burden in calculating coefficients, so that it may not be suitable for the implementation of frequency-adaptive flux observer (FAO).

In the approximation-based methods, the Tustin method is often preferred to reduce the discretization error [25]. Nevertheless, in the process of discretization, the filter structure loses its simplicity of the cascaded integrator. Moreover, even the Tustin method may cause a non-negligible phase shift and magnitude error depending on the filter structure [29].

This paper analyzes the discretization error of the FAO in [20]. In contrast to the ideal operation in the continuous-time domain, the discretization of the FAO deteriorates the performance and may provide an erroneous flux estimation. This discretization error would not be conspicuously improved by changing approximation methods. To eliminate this discrepancy in the high-frequency region, this paper proposes an FAO that combines the integrator at the stationary reference frame (SRF) and that at the rotor reference frame (RRF). To obtain the accurate stator flux information from the output voltage, the backward Euler method at the SRF is selected for the primitive flux calculation. The voltage output delay due to pulse-width-modulation (PWM) is considered for the low-sampling-ratio operation [30]. On the other hand, a frequency-adaptive filter constructed at the RRF is adopted for the fundamental flux extraction. Thanks to the coordinate transformation, the proposed FAO estimates accurately the fundamental stator flux even in the high-frequency region.

The proposed flux observer has the identical transfer function with FAO in [20] at the continuous-time domain. The phase and gain at target frequency are preserved even after the discretization. Unlike [25], the proposed flux observer in the discrete-time domain adopts only backward and forward Euler methods, not Tustin methods, which keep the simple structure as that in the continuous-time domain. The effectiveness of the proposed flux observer is analyzed through the complex transfer function [31] and verified with the simulation and experiments with an IPMSM.

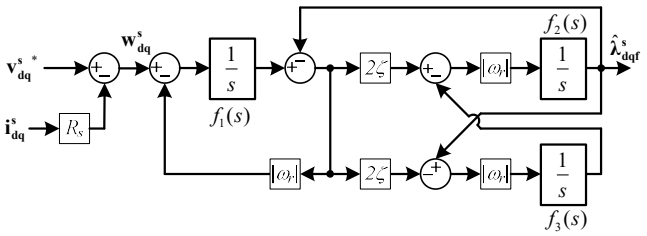

Fig. 1. Block diagram of FAO in [20].

II. Frequency-Adaptive Flux Observer

A. Analysis in Continuous-Time Domain

The stator voltage equation of a PMSM at the stationary reference frame (SRF) can be described as follows.

$$\mathbf{v}^{s}_{dq} = R_s \mathbf{i}^{s}_{dq} + \frac{d}{dt}\boldsymbol{\lambda}^{s}_{dq}. \tag{1}$$

$\mathbf{v}^{s}_{dq}$, $\mathbf{i}^{s}_{dq}$ and $\boldsymbol{\lambda}^{s}_{dq}$ denote stator voltage, stator current, and stator flux, respectively. R_s is the stator resistance. The variables written in the bold stand for the dq-axes complex vector variables, e.g., $\mathbf{v}^{s}_{dq} = v^{s}_{d} + jv^{s}_{q}$. From (1), the stator flux can be expressed with the integral of back-EMF as

$$\boldsymbol{\lambda}^{s}_{dq} = \int\left(\mathbf{v}^{s}_{dq} - R_s \mathbf{i}^{s}_{dq}\right)dt. \tag{2}$$

Although the fundamental stator flux can be calculated using the pure integrator, dc drift and initial condition error should be appropriately handled in the pure integrator. Besides, the low-order harmonics caused by inverter non-linearity and spatial harmonics of PMSM should be sufficiently suppressed.

In [27], the frequency-adaptive circle-tracking observer (FACTO) was developed for the grid-synchronization. Taking advantage of the disturbance rejection property in FACTO, [20] proposed the FAO, of which the block diagram is shown in Fig. 1. In Fig. 1, $\mathbf{w}^{s}_{dq}$ and $\hat{\boldsymbol{\lambda}}^{s}_{dqf}$ are the back EMF and the estimated fundamental stator flux, respectively. ω_r and ζ stand for the electrical rotor speed and damping ratio. In this paper, it is assumed that ω_r can be accurately obtained by a speed sensor or a speed estimator. FAO consists of three integrators, $f_1(s)$, $f_2(s)$, and $f_3(s)$. Although all three integrators participate in disturbance rejection, $f_1(s)$ is the main integrator that integrates the back EMF to calculate the stator flux. The transfer function from $\mathbf{w}^{s}_{dq}$ to $\hat{\boldsymbol{\lambda}}^{s}_{dqf}$ can be calculated as

$$\frac{\hat{\boldsymbol{\lambda}}^{s}_{dqf}}{\mathbf{w}^{s}_{dq}} = \mathbf{H}_S(s) = \frac{2\zeta|\omega_r|}{s^2 + 2\zeta|\omega_r|s + \omega_r^2} = \frac{1}{s}\left(\frac{2\zeta|\omega_r|s}{s^2 + 2\zeta|\omega_r|s + \omega_r^2}\right). \tag{3}$$

It can be noticed that $\mathbf{H}_S(s)$ is an integral filter cascaded with a band-pass filter (BPF). Thus, it functions as a pure integrator at the operating frequency, while rejecting the other frequency components such as dc and fifth and seventh harmonics. In $\mathbf{H}_S(s)$, the absolute value of ω_r is used to keep stability even with the negative ω_r. Fig. 2 depicts the Bode plot of $\mathbf{H}_S(s)$ at various operating frequencies, where ζ is set as 0.707. Each plot has the

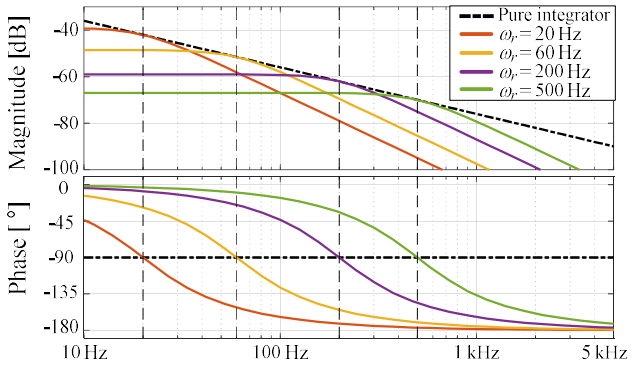

Fig. 2. Bode plot of FAO in [20] at various operating frequencies.

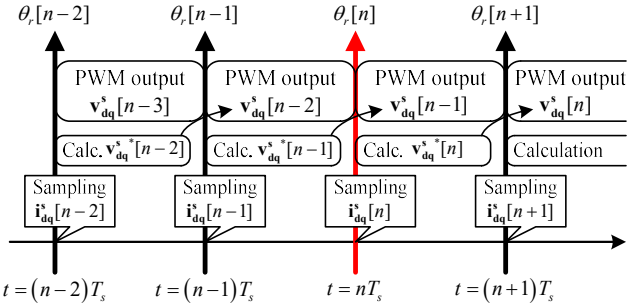

Fig. 3. Time sequence of sampling, calculation, and PWM output.

gain of $1/\omega_r$ with the phase delay of 90° at its operating frequency, like a pure integrator. Other than the operating frequency, both high-frequency and dc components are suppressed by the cascaded BPF.

As discussed in [20], ζ is a tuning factor that determines the disturbance rejection property and the dynamic response. The larger ζ would allow more disturbances in the flux estimation, but the dynamic performance would also be enhanced at the change of the operating condition. In contrast, an excessively small ζ would make the system sensitive to the estimation error of the rotor speed. In practice, ζ is set to a value between 0.1 and unity, considering the desired filtering performance and transient response.

B. Effect of PWM Delay on Stator Flux

Before discretizing the FAO, the behavior of the PWM output delay in the digital signal processor (DSP) should be analyzed. The timing chart of current sampling and PWM output is shown in Fig. 3 [30]. θ_r and T_s denote the electrical rotor angle and the sampling period, respectively. When a DSP controls a PMSM, there is an inevitable delay between current sampling and PWM output due to the control algorithm's computation time. Therefore, the voltage reference calculated at n-th sampling time, i.e., $\mathbf{v}^{s*}_{dq}[n]$, would be synthesized by PWM in the next time period t=[$(n$+1$)T_s$, $(n$+2$)T_s$]. Followingly from (2), the stator flux at n-th sampling $\boldsymbol{\lambda}^s_{dq}[n]$ can be calculated from $\boldsymbol{\lambda}^s_{dq}[n-1]$ and the output voltage in the time period t=[$(n$−1$)T_s$, nT_s] as follows.

$$\boldsymbol{\lambda}^s_{dq}[n]=\boldsymbol{\lambda}^s_{dq}[n-1]+\int_{(n-1)T_s}^{nT_s}\left(\mathbf{v}^s_{dq}-R_s\mathbf{i}^s_{dq}\right)dt\,. \tag{4}$$

The output voltage synthesized in t=[$(n$−1$)T_s$, nT_s] would be the voltage reference calculated at (n−2)-th sampling time, i.e., $\mathbf{v}^{s*}_{dq}[n-2]$. If the inverter non-linearity effect is well-decoupled through an appropriate compensation algorithm, the accurate voltage synthesis can be assumed and (4) can be rewritten as

$$\boldsymbol{\lambda}^s_{dq}[n]=\boldsymbol{\lambda}^s_{dq}[n-1]+T_s\mathbf{v}^{s*}_{dq}[n-2]-\int_{(n-1)T_s}^{nT_s}R_s\mathbf{i}^s_{dq}dt\,. \tag{5}$$

Since the resistive drop would be much smaller than back EMF in most operating conditions, (5) can be simplified as

$$\boldsymbol{\lambda}^s_{dq}[n]=\boldsymbol{\lambda}^s_{dq}[n-1]+T_s\left(\mathbf{v}^{s*}_{dq}[n-2]-R_s\mathbf{i}^s_{dq}[n]\right). \tag{6}$$

Eq. (6) can be described with z-variable as follows for the discrete-time system analysis.

$$\boldsymbol{\lambda}^s_{dq}=\frac{T_sz}{z-1}\left(z^{-2}\mathbf{v}^{s*}_{dq}-R_s\mathbf{i}^s_{dq}\right). \tag{7}$$

It should be noted that the stator flux at each sampling is the backward Euler integration of back EMF, not continuous-time integrator $1/s$. Thus, an ideal discrete-time flux observer also should emulate not $1/s$ nor the Tustin method but the backward Euler integration at the rotor speed.

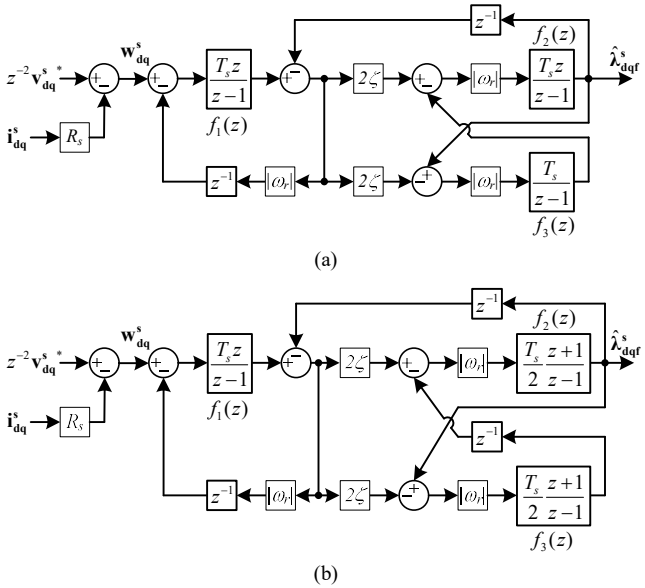

Fig. 4. Block diagram of candidates for discrete-time FAO (DFAO).
(a) DFAO1 ($f_2(s)$: Backward Euler method, $f_3(s)$: Forward Euler method).
(b) DFAO2 ($f_2(s)$: Tustin method, $f_3(s)$: Tustin method with output delay).

C. Discretization of FAO

FAO in [20] has advantages in its simplicity and intuitive implementation. To exploit the virtue of FAO, the discretization methods keeping the structure of double integrators are considered as the comparative group in this paper.

Observing Fig. 1, FAO in [20] consists of three integrators and several feedback loops. Considering that the continuous-time integrator can be approximated with backward, forward, and Tustin methods, there would be 27 design candidates in total, selecting one of three approximation methods for each integrator. However, as discussed in the previous section, the main integrator $f_1(s)$ should be implemented with the backward Euler method to reflect the discretized PWM output. Moreover, since $f_2(s)$ and $f_3(s)$ are cross-coupled with the feedback loop, at least one integrator should contain a delay term z^{-1} to avoid the

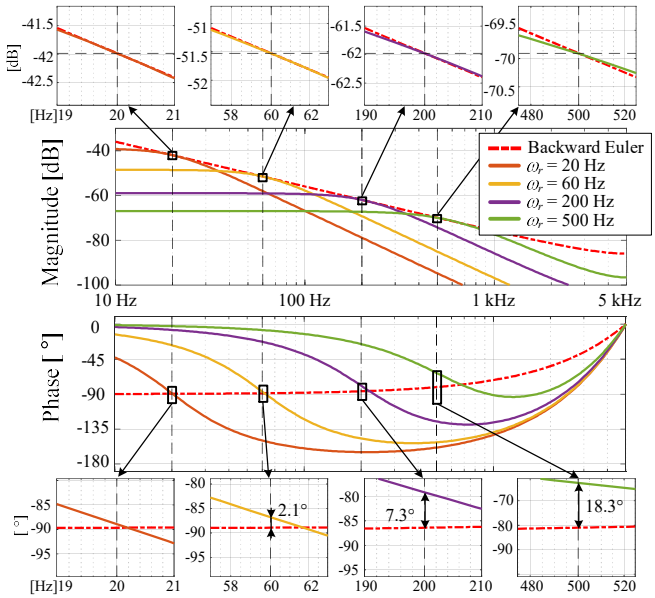

Fig. 5. Bode plot of DFAO1 with various ω_r.

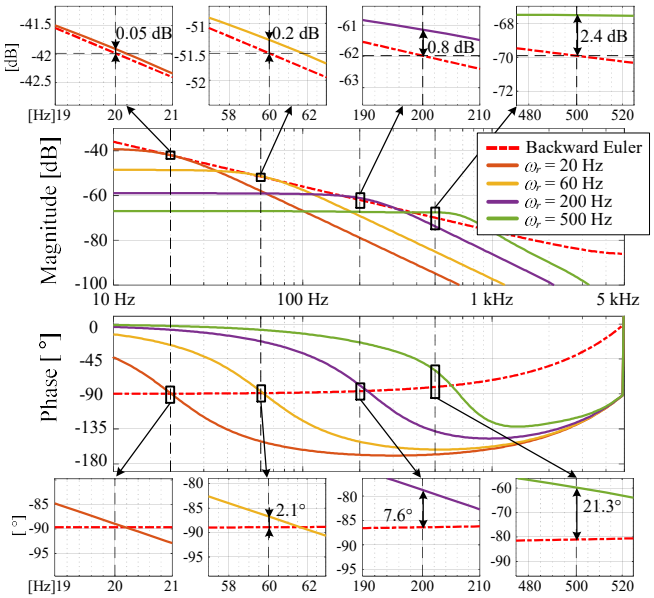

Fig. 6. Bode plot of DFAO2 with various ω_r.

algebraic loop in digital implementation. And, $f_2(s)$ should be Tustin or backward Euler to avoid unit delay in flux estimation output.

Regarding these constraints, two realizable discrete design candidates are shown in Fig. 4. Fig. 4 (a) shows the discrete-time FAO (DFAO), which can be intuitively developed. $f_1(z)$ and $f_2(z)$, which are the main flux calculation path, are set as backward Euler methods to minimize the time delay in flux estimation while adopting forward methods in $f_3(z)$ to avoid the algebraic loop problem in implementation. On the other hand, Fig. 4 (b) shows the alternative design which utilizes Tustin methods. To cut the algebraic loop between $f_2(z)$ and $f_3(z)$, z^{-1} is added between the output of $f_3(z)$ and the input of $f_2(z)$. For ease of explanation, the DFAOs in Fig. 4 (a) and (b) are named as DFAO1 and DFAO2, respectively, in this paper.

The characteristics of DFAO1 and DFAO2 can be analyzed in the z-domain. Firstly, the discrete-time transfer function of DFAO1, $\mathbf{H_{D1}}(z)$, can be calculated as

$$\frac{\hat{\boldsymbol{\lambda}}^{s}_{dqf}}{\mathbf{w}^{s}_{dq}} = \mathbf{H}_{D1}(z) = \frac{2\zeta\left(f_z z\right)^2 |\omega_r|}{1 + 2\zeta f_z |\omega_r| + \left(f_z \omega_r\right)^2 z} \tag{8}$$

where f_z is the forward Euler integrator, $f_z = T_s/(z\text{-}1)$. The backward Euler integrator can be denoted as $f_z z$. Similarly, the discrete-time transfer function of DFAO2 also can be deduced as follows.

$$\frac{\hat{\boldsymbol{\lambda}}^{s}_{dqf}}{\mathbf{w}^{s}_{dq}} = \mathbf{H}_{D2}(z) = \frac{2\zeta f_z g_z z^2 |\omega_r|}{\dfrac{z + z f_z |\omega_r|}{z + g_z |\omega_r|}\left(z + \left(g_z \omega_r\right)^2\right) + 2\zeta g_z |\omega_r|} \tag{9}$$

where g_z is the Tustin integrator, $g_z = 0.5T_s(z+1)/(z\text{-}1)$.

Meanwhile, z-variable can be equivalently converted to s-variable using the following equation.

$$z = \exp(sT_s) \tag{10}$$

where exp(x) is the exponential of x. Using (10), the Bode plots of DFAO1 and DFAO2 could be drawn in the s-domain. Fig. 5 shows the Bode plot of DFAO1 at 10 kHz of the sampling frequency. Observing the magnitude plot at the top of Fig. 5,

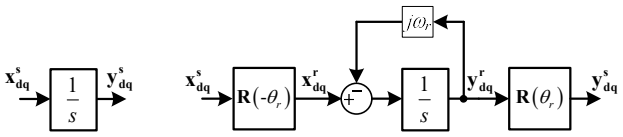

(a) (b)

Fig. 7. (a) Integrator designed at SRF. (b) Integrator designed at RRF.

DFAO1 well corresponds with the backward Euler methods at operating frequency even at high speeds. However, as the speed increases, the phase of DFAO1 is distorted, as the speed increases. Although the phase delay at 20 Hz of operating frequency is well-matched with the backward Euler method, the discrepancy in phase delay increases to 18.3° at 500 Hz of operating frequency. This phase error affects directly the fundamental flux estimation, and the estimated flux vector would also have the phase error, which could deteriorate the control performance. The Bode plot of DFAO2 is depicted in Fig. 6. DFAO2 not only increases the angle discrepancy but also has a non-negligible magnitude error. When the operating frequency is at 500 Hz, the magnitude error would be 2.4 dB, which would induce more than 30 % error, compared to the desired flux magnitude.

As shown in Fig. 5 and Fig. 6, the direct replacement from the ideal integrator to the discrete integration method does not secure sufficient accuracy in fundamental flux estimation, especially at high speeds. This discrepancy comes from the discretization error of the integrator. In the low-frequency region, the difference between the discrete integrator and the ideal integrator $1/s$ would not be considerable. However, no matter what type of approximation method is used, it would not precisely emulate $1/s$ at a higher operating frequency. This limitation of the discrete integrator results in the phase and magnitude errors in FAO.

III. Proposed FAO at RRF

The FAO in [20] was designed at the SRF. As a result, all the

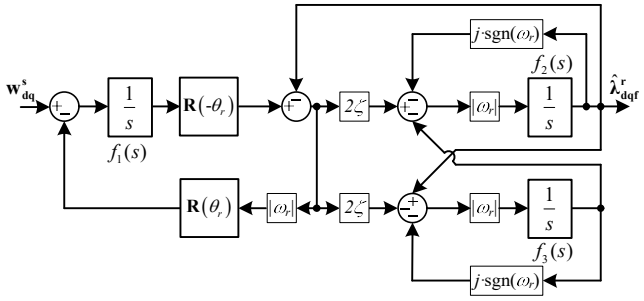

Fig. 8. Block diagram of FAO at RRF.

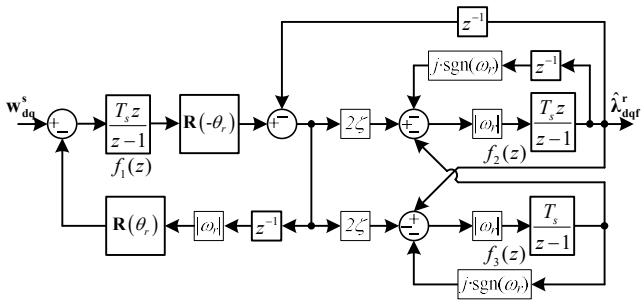

Fig. 9. Block diagram of the proposed DFAO at RRF (DRFAO).

inputs of each integrator would be the ac signals rotating with ω_r, which leads to the integration error compared to the continuous-time integration. As aforementioned, the feedback terms of the DFAOs require at least a unit delay to avoid the algebraic loop in the implementation, although the feedback terms in continuous-time are assumed to be calculated instantaneously in real time. Since the fundamental flux at the SRF is the rotating signal, the delay in the feedback loop also makes the ideal operation difficult.

Meanwhile, any variable at SRF, e.g., $\mathbf{x}^{s}_{dq}$, can be expressed at RRF with the electrical rotor angle θ_r as follows.

$$\mathbf{x}^{r}_{dq} = \mathbf{R}(-\theta_r)\mathbf{x}^{s}_{dq} \tag{11}$$

where $\mathbf{R}(\theta)$ is the rotational operator, i.e., $\mathbf{R}(\theta)=\exp(j\theta)$. Fig. 7 (a) depicts the integrator block. This ideal integrator at SRF also can be described at RRF as shown in Fig. 7 (b). It should be noted that the integrator in Fig. 7 (b) works the same as the ideal integrator $1/s$. However, the input of the $1/s$ in Fig. 7 (b) is not $\mathbf{x}^{s}_{dq}$ but $\mathbf{x}^{r}_{dq}$, which is the dc signal at the steady state.

Using the integrator in Fig. 7 (b), the FAO in [20] can be reconstructed as shown in Fig. 8. The sgn(ω) stands for the sign function, which can be defined as

$$\mathrm{sgn}(\omega)=\begin{cases}1, & \text{if } \omega \ge 0,\\ -1, & \text{if } \omega < 0.\end{cases} \tag{12}$$

In Fig. 8, the rotational operators originated from $f_1(s)$ and $f_2(s)$ are unified thanks to the commutative and distributive properties of linear system. It provides structural simplicity and relieves the calculation burden. The FAO at RRF calculates the stator flux at RRF, which can be expressed at SRF as follows.

$$\hat{\boldsymbol{\lambda}}^{s}_{dq} = \mathbf{R}(\theta_r)\hat{\boldsymbol{\lambda}}^{r}_{dq}. \tag{13}$$

The FAO in Fig. 8 is the same FAO in [20], in which only the $f_2(s)$ and $f_3(s)$ are replaced with the integrators at RRF in Fig. 7 (b). Therefore, the transfer function from $\mathbf{w}^{s}_{dq}$ to $\hat{\boldsymbol{\lambda}}^{s}_{dqf}$ would be identical to (3).

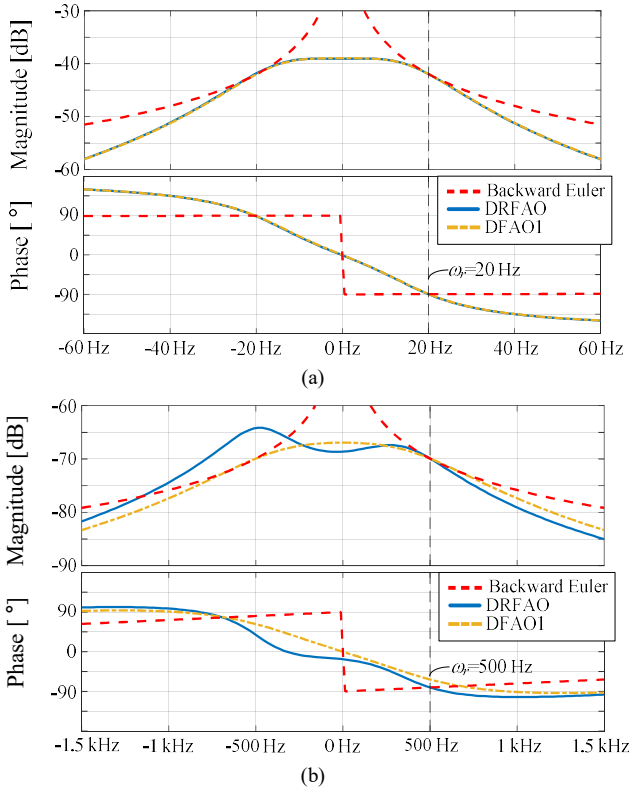

Fig. 10. FRF of the various DFAOs. (a) ω_r=20 Hz. (b) ω_r=500 Hz.

The proposed FAO at RRF can be implemented in the z-domain based on the backward Euler methods, as depicted in Fig. 9. In this paper, the proposed DFAO at RRF is denoted as DRFAO. For the simple implementation, all integrators are set to backward Euler methods, and the unit delay z^{-1} is added to all the feedback terms. In the case of $f_3(z)$, the z^{-1} and the backward Euler integrator are integrated as the forward Euler integrator.

Unlike that the fundamental-frequency-components in the conventional DFAOs are the rotating signals, those in the proposed DRFAO are transformed to the dc signals at the steady state. Thus, the unit delays in the feedback loop would not disturb the fundamental flux estimation of the proposed DRFAO.

Since the proposed DRFAO includes the dq-axis cross-coupling term, it can be analyzed based on the complex transfer function in [20] and [31]. The transfer function from $\mathbf{w}^{s}_{dq}$ to $\hat{\boldsymbol{\lambda}}^{s}_{dqf}$ in the proposed DRFAO can be represented as follows.

$$\frac{\hat{\boldsymbol{\lambda}}^{s}_{dqf}}{\mathbf{w}^{s}_{dq}} = \mathbf{H}_{DR}(z) = \frac{2\zeta\left(f_z z\right)^2 \mathbf{q}|\omega_r|}{\left(\mathbf{q}+f_z|\omega_r|\right)\dfrac{f_z\left(1+z\mathbf{q}\left(\omega_r\mathbf{h}_z\right)^2\right)}{\mathbf{q}\mathbf{h}_z\left(1+|\omega_r|\mathbf{h}_z\right)}+2\zeta f_z|\omega_r|} \tag{14}$$

where

$$\mathbf{h}_z = \frac{T_s}{(z-\mathbf{p})\mathbf{q}}, \tag{15}$$

$$\mathbf{p} = \left(\cos(\omega_r T_s)+j\cdot\sin(\omega_r T_s)\right)(1-j\cdot\omega_r T_s), \tag{16}$$

$$\mathbf{q} = \cos(\omega_r T_s)-j\cdot\sin(\omega_r T_s). \tag{17}$$

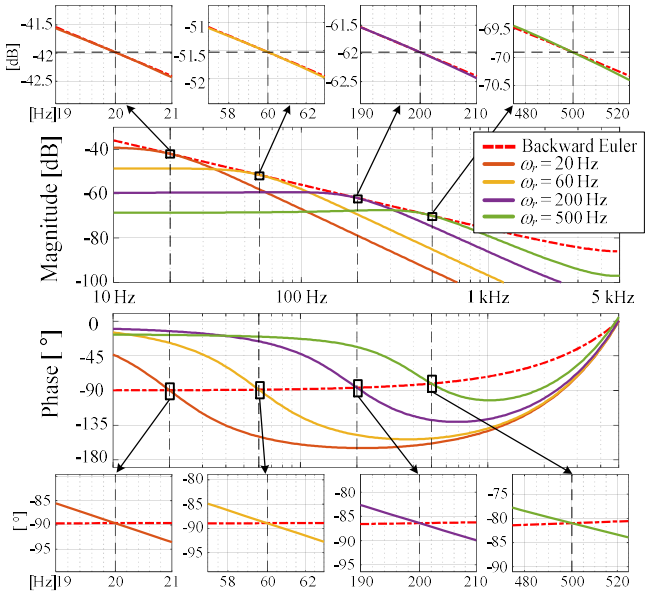

Fig. 11. Bode plot of DRFAO at various operating frequencies.

In (14)-(17), **p**, **q**, and $\mathbf{h}_z$ are the complex vectors associated with ω_r. When ω_r is much smaller than the sampling frequency f_{samp}, both **p** and **q** would converge to the unity, and $\mathbf{h}_z$ would be close to f_z. Accordingly, $\mathbf{H}_{DR}(z)$ in (14) would be approximated to $\mathbf{H}_{D1}(z)$ in (8) at the low-speed.

Unlike the transfer function with real-number coefficients, the complex transfer function would have a different Bode plot at the negative frequency with that of the positive frequency [20]. To depict the negative frequency domain, the frequency-response function (FRF) of the proposed DRFAO is plotted in Fig. 10 at the condition of f_{samp}=10 kHz, ζ=0.707. At ω_r=20 Hz, the frequency response of DRFAO is close to that of DFAO1 and both are symmetric at the positive and negative frequencies. At ω_r=500 Hz, DFAO1 keeps the symmetry but the phase differs from the backward Euler method at the operating frequency, which provokes the fundamental flux errors. In contrast, the phase of the proposed DRFAO crosses the backward Euler method exactly at ω_r, which estimates the positive sequence component of fundamental flux without an error. But, it has the asymmetric gain in the negative frequency region.

The gain error of the proposed DRFAO is maximized by 6 dB at $-\omega_r$, which corresponds to the negative sequence component. Thus, the proposed DRFAO would allow more turbulences in the flux estimation for a faulty PMSM, which has a considerable negative sequence component in $\boldsymbol{\lambda}^{s}_{dqf}$. However, the negative sequence of $\boldsymbol{\lambda}^{s}_{dqf}$ would be negligible in most healthy PMSMs, due to their electrical symmetry.

Since the main flux vector rotates with ω_r, it is important to confirm whether $\mathbf{H}_{DR}(\exp(j\omega_r T_s))$ is well-matched with the backward Euler integrator, rather than to check whether $\mathbf{H}_{DR}(\exp(-j\omega_r T_s))$ does. To explore the discrepancy between DRFAO and backward Euler method at ω_r, Bode plots for various ω_r are drawn in Fig. 11. Unlike the Bode plots of DFAO1 and DFAO2, it is rarely found the error between the DRFAO and backward Euler at ω_r.

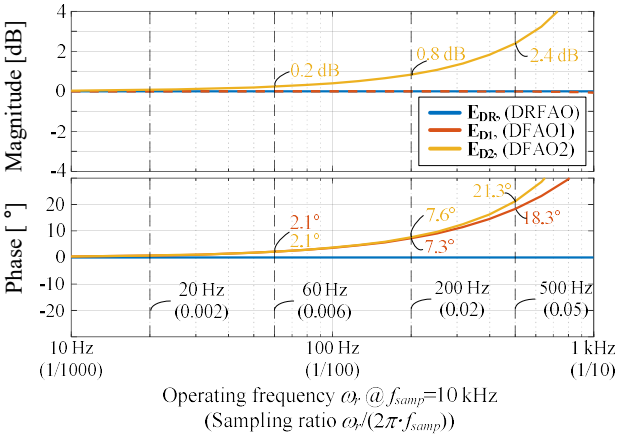

Fig. 12. Magnitude and phase errors of DFAO1, DFAO2, and DRFAO.

The magnitude and phase error of the proposed method at an arbitrary operating frequency can be evaluated quantitatively. Since the magnitude and phase at an operating frequency ω_r can be calculated as $\mathbf{H}_{DR}(\exp(j\omega_r T_s))$, the magnitude and phase errors of DRFAO compared to the backward Euler method can be derived with complex variables $\mathbf{E}_{DR}$ as follows.

$$\mathbf{E}_{DR}(\omega_r) = \left(\frac{\mathbf{H}_{DR}(z)}{f_z z} \right) \Bigg|_{z=\exp(j\omega_r T_s)} . \tag{18}$$

Observing (14), it is noted that $\mathbf{H}_{DR}(\exp(j\omega_r T_s))$ is identical to the backward Euler method at $z=\exp(j\omega_r T_s)$ as follows.

$$\mathbf{H}_{DR}\left(\exp\left(j\omega_r T_s\right)\right) = \frac{T_s \exp\left(j\omega_r T_s\right)}{\exp\left(j\omega_r T_s\right) - 1} . \tag{19}$$

Therefore, $\mathbf{E}_{DR}$ is the unity regardless of the operating speed, and the magnitude and phase of DRFAO at the operating frequency are identical to those of the backward Euler integrator. Similarly, the magnitude and phase errors of DFAO1 and DFAO2 can be evaluated with

$$\mathbf{E}_{D1}(\omega_r) = \left(\frac{\mathbf{H}_{D1}(z)}{f_z z} \right) \Bigg|_{z=\exp(j\omega_r T_s)} , \tag{20}$$

$$\mathbf{E}_{D2}(\omega_r) = \left(\frac{\mathbf{H}_{D2}(z)}{f_z z} \right) \Bigg|_{z=\exp(j\omega_r T_s)} . \tag{21}$$

Fig. 12 shows the magnitude and phase errors of the DFAOs according to ω_r. Since (20) and (21) can be expressed with functions of $\omega_r T_s$, the changes in f_{samp} and ω_r can be interpreted as the variation in the sampling ratio, i.e., $\omega_r/(2\pi f_{samp})$. Thus, the sampling ratio is also shown in the x-axis of Fig. 12. As seen in Fig. 5 and Fig. 6, the errors of DFAO1 and DFAO 2 increase in the high frequency region. However, the proposed DRFAO has a consistent performance without errors.

IV. Simulation and Experimental Results

To verify the effectiveness of the proposed method, simulation and experiments have been conducted. The target IPMSM is shown in Fig. 13, and the system parameters are listed in Table I. The motor parameters extracted by finite element analysis (FEA) have been used in the simulation [32],

TABLE I. SYSTEM SPECIFICATIONS AND NOMINAL MOTOR PARAMETERS

Number of pole pairs, p	4	
Base speed	3000	r/min
Rated torque	4.03	N·m
Rated current	5.2	A_{rms}
Back-EMF constant, λ_f	88.1	mWb
Stator resistance, R_s	0.85	Ω
d-axis inductance, L_{ds}	8	mH
q-axis inductance, L_{qs}	12	mH
Damping coefficient, ζ	0.707	
DC link voltage, V_{dc}	311	V
Switching frequency, f_{sw}	10	kHz
Sampling frequency, f_{samp}	10	kHz
Dead time, T_{dead}	2	μs

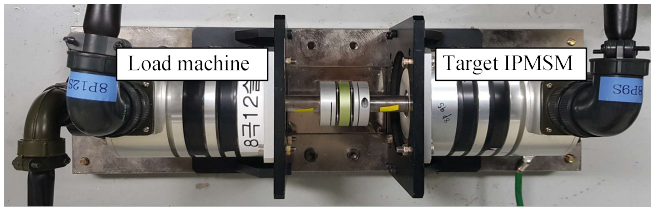

Fig. 13. Motor-generator set.

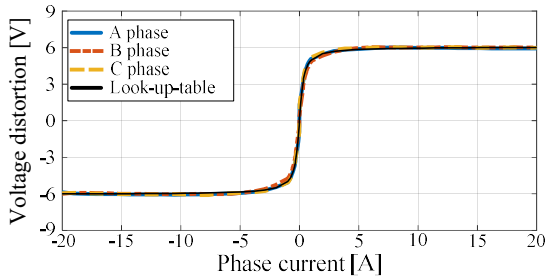

Fig. 14. Pole voltage distortion due to inverter non-linearity effect (f_{sw}=10 kHz).

and it has been simulated by MATLAB Simulink. In the experiments, the control algorithm has been implemented on TMS320F28377, and output current and dc-link voltage have been measured for the current control. The rotor speed information is obtained through the state observer in [33], where the bandwidth is set to 100 Hz.

In both the simulation and the experiments, the switching frequency is set as 10 kHz with the single sampling at each switching period, and the current control bandwidth is set as 250 Hz, unless otherwise stated. In the experimental setup, the dead time is set as 2 μs, and FS50R12KT4_B15 is used for the power device. Besides the proposed DRFAO, DFAO1 and DFAO2 are also implemented for comparison. The target motor operates with torque control mode on the maximum torque per Ampere (MTPA) current trajectory.

In the experimental setup, the inverter non-linearity effects such as on-drop voltage of power device and pole voltage distortion due to dead-time effect have been measured through a pretest and compensated by a feedforward term in the voltage reference [34], [35]. The linear voltage drop proportional to phase current is treated as an equivalent stator resistance, and the nonlinear voltage distortion is decoupled by a premade look-up-table (LUT). Fig. 14 depicts the measured pole voltage

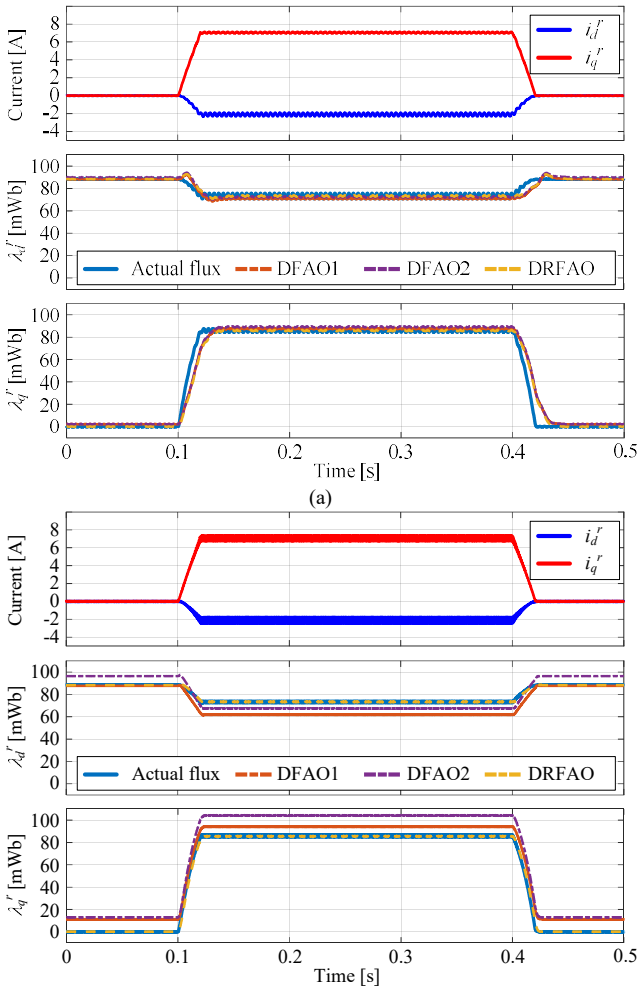

Fig. 15. Simulation 1: Flux estimation under torque variation (f_{samp}=10 kHz). (a) ω_r=40 Hz. (b) ω_r=200 Hz.

distortion of the inverter. The compensation LUT is constructed by averaging the voltage distortion of each phase. The voltage distortion above a certain current level barely changes, while it has a steep gradient near zero-current region. Thus, the feedforward-based inverter non-linearity compensation provides satisfactory performance in overall operating conditions except for near the zero-current region.

A. Simulation Results

Fig. 15 depicts the flux estimation under the torque reference change. The rated torque is applied from 0.1 s to 0.4 s with the slew rate of 50 pu/s. In Fig. 15 (a), all three DFAOs show a similar dynamic performance and converge to the actual flux vector when ω_r= 40 Hz. However, when ω_r=200 Hz, only the proposed DRFAO estimates the actual flux without an error, while the flux estimation of DFAO1 and DFAO2 are erroneous at the steady state. It should be noted that the dynamic performance of the proposed DRFAO is not degraded compared to those of the conventional DFAOs.

Focusing on the effect of speed variation, Fig. 16 (a)-(c) show the performance of DFAOs according to the operating speed from 20 Hz to 200 Hz. Fig. 16 (a), (b), and (c) are the flux waveforms at no load, 50 % load, and full load conditions,

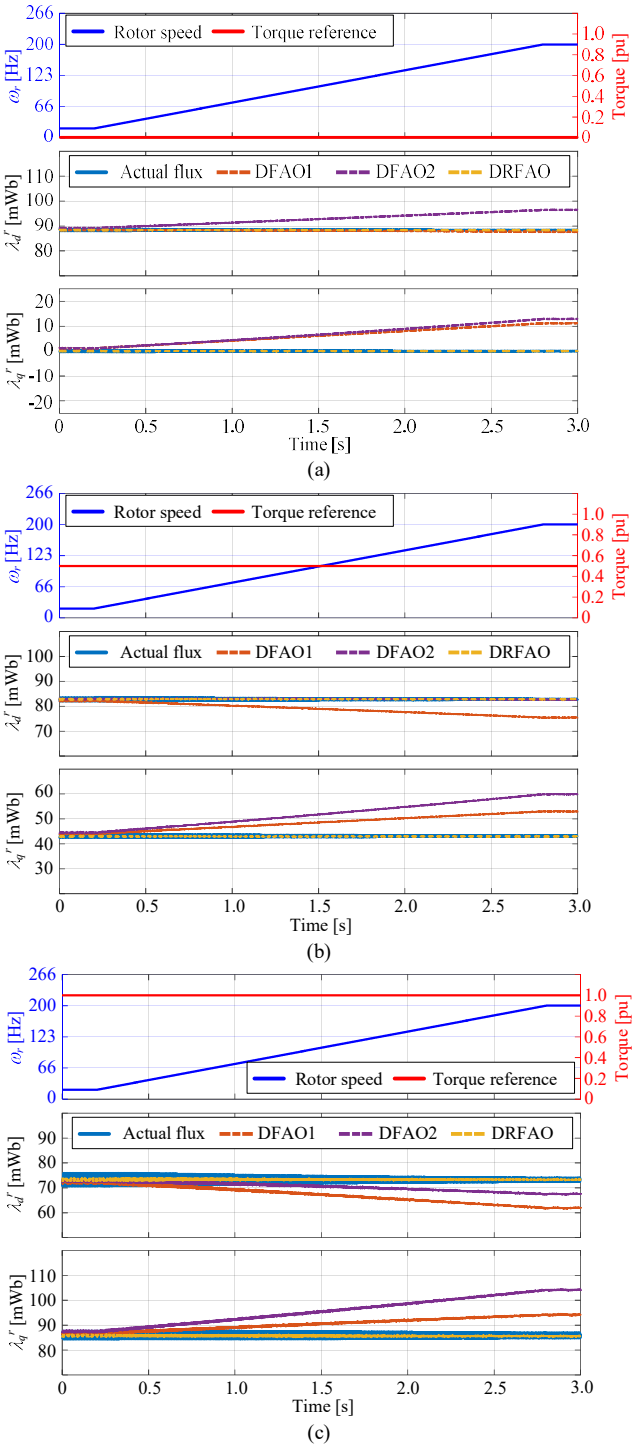

Fig. 16. Simulation 2: Flux estimation under speed variation (f_{samp}=10 kHz). (a) No load. (b) 50% load. (c) Full load.

respectively. The actual stator flux vector at no load is nothing but the flux linkage of the permanent magnet, which would be 88.4 mWb on *d*-axis. As the load increases, *q*-axis flux λ_q^r also increases from null to 87 mWb while *d*-axis flux λ_d^r slightly decreases due to MTPA operation. As seen in Fig. 15, all three DFAOs provide an accurate flux estimation around 20 Hz. However, the discrepancy between the actual flux and the flux estimation of DFAO1 and DFAO2 is worsened, as the speed increases. In contrast, DRFAO keeps the estimation of the

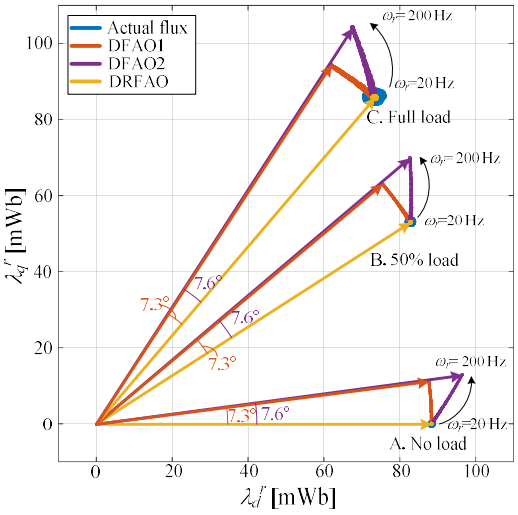

Fig. 17. Lissajous waveforms of Simulation 2 (f_{samp}=10 kHz).

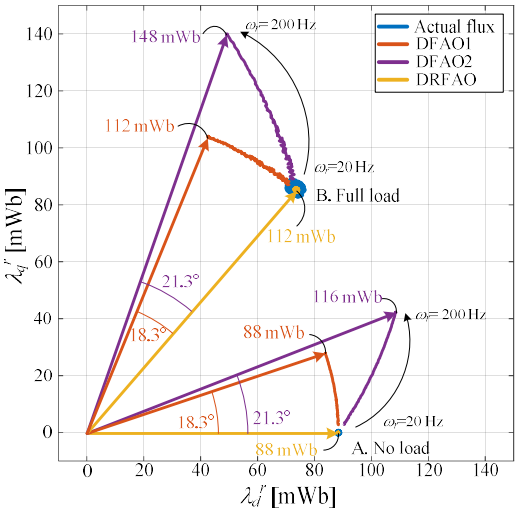

Fig. 18. Lissajous waveforms of Simulation 2 (f_{samp}=4 kHz).

fundamental flux without an error even at 200 Hz, regardless of the load condition.

The flux estimation error of the conventional DFAOs can be analyzed through the Lissajous waveforms, as shown in Fig. 17. The angle discrepancies of DFAO1 and DFAO2 are 7.3° and 7.6°, regardless of the load conditions. And, DFAO1 barely has the magnitude error, while the DFAO2 overestimates the flux magnitude compared to the actual flux. These results agree well with the analysis in Section II. *C*.

To see the effect of the sampling frequency change, the flux estimation under f_{samp}=4 kHz is shown in Fig. 18. Since f_{samp} is reduced from 10 kHz to 4 kHz, changing ω_r from 20 Hz to 200 Hz would correspond to changing the sampling ratio from 0.005 to 0.05. Therefore, the discretization errors in DFAO1 and DFAO2 increase, and the errors at ω_r=200 Hz well-correspond to Fig. 13. In contrast, even at the low f_{samp}, the proposed DRFAO accurately estimates the flux without an error.

B. Experimental Results

Fig. 19 depicts the experimental waveforms under torque reference change. The rated torque is applied from 0.1 s to 0.4 s with the slope of 50 pu/s. Similar to the simulation results,

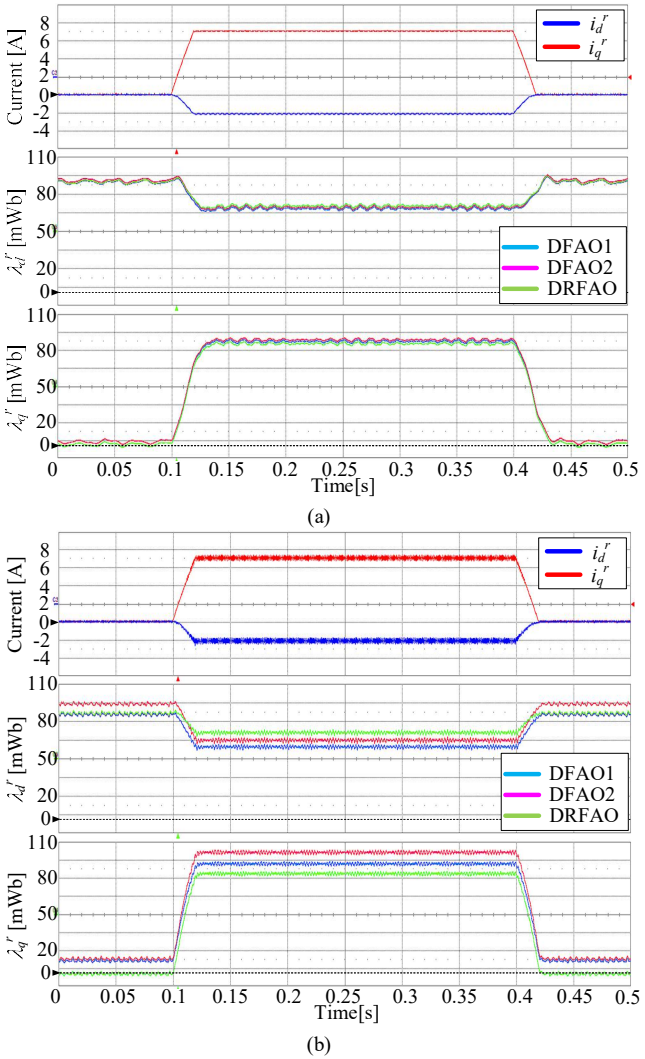

Fig. 19. Experiments 1: Flux estimation under torque variation (f_{samp}=10 kHz). (a) ω_r=40 Hz. (b) ω_r=200 Hz.

DFAO1, DFAO2, and the proposed DRFAO have equal dynamic performance and converge to an almost identical point at a steady state. Due to the frequency-adaptive characteristic, the dynamic performance at ω_r=40 Hz is a little slower than that at ω_r=200 Hz. In Fig. 19 (b), the proposed DRFAO estimates the same flux vector as at ω_r=40 Hz, while the flux estimation of DFAO1 and DFAO2 differs from those at ω_r=40 Hz.

This discrepancy can be seen more clearly in Fig. 20. Fig. 20 shows the Lissajous waveforms under the speed variation, which corresponds to the simulation results in Fig. 17. The rotor speed is changed from 20 Hz to 200 Hz, while the load condition is set to zero, half, and full load, respectively. Unlike the simulation results in Fig. 16 (a), the flux estimation in no-load condition is oscillatory in low-speed region. It would be caused by the inverter non-linearity, which is not easy to be precisely compensated in zero current region. As shown in B and C in Fig. 20, there are much less oscillations in the estimated flux when the output current is not zero.

As the speed increases to 200 Hz, the phase deviation in DFAO1 and DFAO2 increases up to around 7°, and the magnitude error between DFAO2 and DRFAO is expanded up

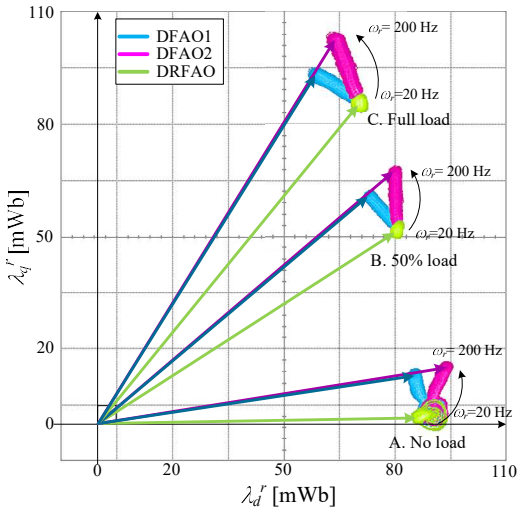

Fig. 20. Lissajous waveforms of Experiments 2: Flux estimation under speed variation (f_{samp}=10 kHz).

to 10 %, which is 0.8 dB. On the other hand, the stator flux estimated by DRFAO is fixed at one point regardless of the speed variation. These results support the analysis in Section II and the simulation results in Fig. 17.

V. Conclusion

This paper analyzes the discretization error in the frequency-adaptive flux observer. Due to the pulse-width-modulation (PWM) and the calculation delay in the digital signal processor, the flux trajectory is formed through the backward Euler integral of stator voltage, not through the continuous-time integral of that. Besides, the accuracy of the flux estimation is deteriorated by the gain and phase discrepancies of the band-pass filters in the frequency-adaptive flux observer caused by the integrator approximation, so that the estimated fundamental flux deviates from the actual flux vector in the high-speed region.

To mitigate the discretization error at the high operating frequencies, this paper proposes the frequency-adaptive flux observer that combines the integrator at the stationary reference frame and those at the rotor reference frame. In the proposed flux observer, the backward Euler integrator at the stationary reference frame calculates the primitive stator flux considering the delay of PWM. In addition, the fundamental stator flux information is extracted by the frequency adaptive filter constructed at the rotor reference frame. Since all the inputs are dc signals in the proposed frequency-adaptive filter, even the discrete-time integrator can accurately emulate the ideal integral. Through the reference frame change, the gain and cutoff frequency of a band-pass filter can be preserved in the proposed flux observer. Consequently, the proposed method shows consistent performance against the speed variation. The effectiveness of the proposed method is verified with the simulation and experimental results.

References

[1] M. Hinkkanen and J. Luomi, "Modified integrator for voltage model flux estimation of induction motors," in *IEEE Transactions on Industrial Electronics*, vol. 50, no. 4, pp. 818-820, Aug. 2003.

[2] J. Yoo, J. Lee and S. Sul, "Design of Full-Order Flux Observer for Induction Motor Drive Robust to Rotor Time Constant Variation," *2019 10th International Conference on Power Electronics and ECCE Asia (ICPE 2019 - ECCE Asia)*, Busan, Korea (South), 2019, pp. 1-6.

[3] A. Varatharajan, G. Pellegrino and E. Armando, "Sensorless Synchronous Reluctance Motor Drives: Auxiliary Flux based Position Observer," in *IEEE Journal of Emerging and Selected Topics in Power Electronics*.

[4] J. Yoo, Y. Lee and S. Sul, "Back-EMF Based Sensorless Control of IPMSM with Enhanced Torque Accuracy Against Parameter Variation," *2018 IEEE Energy Conversion Congress and Exposition (ECCE)*, Portland, OR, 2018, pp. 3463-3469.

[5] T. G. Habetler, F. Profumo, G. Griva, M. Pastorelli and A. Bettini, "Stator resistance tuning in a stator-flux field-oriented drive using an instantaneous hybrid flux estimator," in *IEEE Transactions on Power Electronics*, vol. 13, no. 1, pp. 125-133, Jan. 1998.

[6] J. Lee, Y. Kwon and S. Sul, "Experimental Identification of IPMSM Flux-Linkage Considering Spatial Harmonics for High-Accuracy Simulation of IPMSM Drives," *2018 IEEE Energy Conversion Congress and Exposition (ECCE)*, Portland, OR, 2018, pp. 5804-5809.

[7] J. Yoo, J. Lee, S. Sul and N. A. Baloch, "Stator Resistance Estimation Using DC Injection With Reduced Torque Ripple in Induction Motor Sensorless Drives," in *IEEE Transactions on Industry Applications*, vol. 56, no. 4, pp. 3744-3754, July-Aug. 2020.

[8] H. -S. Jung, H. Kim, S. -K. Sul and D. Berry, "Magnet Temperature Estimation of IPMSM by Using Fundamental Reactive Energy Considering Variation of Inductances," in *IEEE Transactions on Power Electronics*.

[9] H. Kim, Y. Lee, S. Sul, J. Yu and J. Oh, "Online MTPA Control of IPMSM Based on Robust Numerical Optimization Technique," in *IEEE Transactions on Industry Applications*, vol. 55, no. 4, pp. 3736-3746, July-Aug. 2019.

[10] H. -S. Kim and S. -K. Sul, "Real-time Torque Control of IPMSM under Flux Variations," in *IEEE Journal of Emerging and Selected Topics in Power Electronics*.

[11] H. Kim and S. Sul, "Online MTPA Operation of IPMSM Based on Dual-Loop Control in Polar Coordinates," *2019 10th International Conference on Power Electronics and ECCE Asia (ICPE 2019 - ECCE Asia)*, Busan, Korea (South), 2019, pp. 1-6.

[12] J. Holtz and Juntao Quan, "Drift- and parameter-compensated flux estimator for persistent zero-stator-frequency operation of sensorless-controlled induction motors," in *IEEE Transactions on Industry Applications*, vol. 39, no. 4, pp. 1052-1060, July-Aug. 2003.

[13] M. Karimi-Ghartemani, S. A. Khajehoddin, P. K. Jain, A. Bakhshai and M. Mojiri, "Addressing DC Component in PLL and Notch Filter Algorithms," in *IEEE Transactions on Power Electronics*, vol. 27, no. 1, pp. 78-86, Jan. 2012.

[14] L. Ben-Brahim and A. Kawamura, "A fully digitized field-oriented controlled induction motor drive using only current sensors," in *IEEE Transactions on Industrial Electronics*, vol. 39, no. 3, pp. 241-249, June 1992.

[15] Myoung-Ho Shin, Dong-Seok Hyun, Soon-Bong Cho and Song-Yul Choe, "An improved stator flux estimation for speed sensorless stator flux orientation control of induction motors," in *IEEE Transactions on Power Electronics*, vol. 15, no. 2, pp. 312-318, March 2000.

[16] G. Jo and J. Choi, "Gopinath Model-Based Voltage Model Flux Observer Design for Field-Oriented Control of Induction Motor," in *IEEE Transactions on Power Electronics*, vol. 34, no. 5, pp. 4581-4592, May 2019.

[17] J. S. Lee, C. Choi, J. Seok and R. D. Lorenz, "Deadbeat-Direct Torque and Flux Control of Interior Permanent Magnet Synchronous Machines With Discrete Time Stator Current and Stator Flux Linkage Observer," in *IEEE Transactions on Industry Applications*, vol. 47, no. 4, pp. 1749-1758, July-Aug. 2011.

[18] Y. Jeong and S. Sul, "Adaptive Flux Observer with On-line Inductance Estimation of an IPMSM Considering Magnetic Saturation," *2005 IEEE 36th Power Electronics Specialists Conference*, Recife, 2005, pp. 2467-2473.

[19] P. L. Jansen and R. D. Lorenz, "A physically insightful approach to the design and accuracy assessment of flux observers for field oriented induction machine drives," in *IEEE Transactions on Industry Applications*, vol. 30, no. 1, pp. 101-110, Jan.-Feb. 1994.

[20] H. Kim, S. Sul, H. Yoo and J. Oh, "Distortion-Minimizing Flux Observer for IPMSM Based on Frequency-Adaptive Observers," in *IEEE Transactions on Power Electronics*, vol. 35, no. 2, pp. 2077-2087, Feb. 2020.

[21] M. Koç, J. Wang and T. Sun, "An Inverter Nonlinearity-Independent Flux Observer for Direct Torque-Controlled High-Performance Interior Permanent Magnet Brushless AC Drives," in *IEEE Transactions on Power Electronics*, vol. 32, no. 1, pp. 490-502, Jan. 2017.

[22] W. Xu and R. D. Lorenz, "Reduced Parameter Sensitivity Stator Flux Linkage Observer in Deadbeat-Direct Torque and Flux Control for IPMSMs," in *IEEE Transactions on Industry Applications*, vol. 50, no. 4, pp. 2626-2636, July-Aug. 2014.

[23] Z. Xin, R. Zhao, F. Blaabjerg, L. Zhang and P. C. Loh, "An Improved Flux Observer for Field-Oriented Control of Induction Motors Based on Dual Second-Order Generalized Integrator Frequency-Locked Loop," in *IEEE Journal of Emerging and Selected Topics in Power Electronics*, vol. 5, no. 1, pp. 513-525, March 2017.

[24] R. Zhao, Z. Xin, P. C. Loh and F. Blaabjerg, "A Novel Flux Estimator Based on Multiple Second-Order Generalized Integrators and Frequency-Locked Loop for Induction Motor Drives," in *IEEE Transactions on Power Electronics*, vol. 32, no. 8, pp. 6286-6296, Aug. 2017.

[25] W. Xu, Y. Jiang, C. Mu and F. Blaabjerg, "Improved Nonlinear Flux Observer-Based Second-Order SOIFO for PMSM Sensorless Control," in *IEEE Transactions on Power Electronics*, vol. 34, no. 1, pp. 565-579, Jan. 2019.

[26] Y. Park and S. Sul, "Sensorless Control Method for PMSM Based on Frequency-Adaptive Disturbance Observer," in *IEEE Journal of Emerging and Selected Topics in Power Electronics*, vol. 2, no. 2, pp. 143-151, June 2014.

[27] Y. Park, H. Kim and S. Sul, "Frequency-Adaptive Observer to Extract AC-Coupled Signals for Grid Synchronization," in *IEEE Transactions on Industry Applications*, vol. 53, no. 1, pp. 273-282, Jan.-Feb. 2017.

[28] M. Ciobotaru, R. Teodorescu and F. Blaabjerg, "A new single-phase PLL structure based on second order generalized integrator," *2006 37th IEEE Power Electronics Specialists Conference*, Jeju, 2006, pp. 1-6.

[29] A. G. Yepes, F. D. Freijedo, J. Doval-Gandoy, Ó. López, J. Malvar and P. Fernandez-Comesaña, "Effects of Discretization Methods on the Performance of Resonant Controllers," in *IEEE Transactions on Power Electronics*, vol. 25, no. 7, pp. 1692-1712, July 2010.

[30] Bon-Ho Bae and Seung-Ki Sul, "A compensation method for time delay of full-digital synchronous frame current regulator of PWM AC drives," in *IEEE Transactions on Industry Applications*, vol. 39, no. 3, pp. 802-810, May-June 2003.

[31] F. Briz, M. W. Degner and R. D. Lorenz, "Analysis and design of current regulators using complex vectors," in *IEEE Transactions on Industry Applications*, vol. 36, no. 3, pp. 817-825, May-June 2000.

[32] X. Chen, J. Wang, B. Sen, P. Lazari and T. Sun, "A High-Fidelity and Computationally Efficient Model for Interior Permanent-Magnet Machines Considering the Magnetic Saturation, Spatial Harmonics, and Iron Loss Effect," in *IEEE Transactions on Industrial Electronics*, vol. 62, no. 7, pp. 4044-4055, July 2015.

[33] R. D. Lorenz and K. W. Van Patten, "High-resolution velocity estimation for all-digital, AC servo drives," in *IEEE Transactions on Industry Applications*, vol. 27, no. 4, pp. 701-705, July-Aug. 1991.

[34] G. Pellegrino, R. I. Bojoi, P. Guglielmi and F. Cupertino, "Accurate Inverter Error Compensation and Related Self-Commissioning Scheme in Sensorless Induction Motor Drives," in *IEEE Transactions on Industry Applications*, vol. 46, no. 5, pp. 1970-1978, Sept.-Oct. 2010.

[35] Y. Park and S. Sul, "A Novel Method Utilizing Trapezoidal Voltage to Compensate for Inverter Nonlinearity," in *IEEE Transactions on Power Electronics*, vol. 27, no. 12, pp. 4837-4846, Dec. 2012.

Jiwon Yoo (S'17) was born in Seoul, South Korea, in 1990. He received the B.S. degree in electrical engineering from Seoul National University, Seoul, South Korea in 2017, where he is currently pursuing the Ph.D. degree in electrical engineering. From 2014 to 2017, He was a Research Engineer with Seoho Electric Company, Anyang, South Korea. His current research interests include power electronics, control of electric machines, power semiconductors, and sensorless drives.

He was the recipient of the Best Paper Award First Prize at 2019 International Conference on Power Electronics (ICPE-Busan/ECCE-Asia) and the Best Paper Award at 2020 International Power Electronics and Motion Control Conference (IPEMC-Nanjing/ECCE-Asia).

Hyeon-Sik Kim (S'14-M'19) was born in Busan, South Korea, in 1988. He received the B.S. and Ph. D. degree in electrical and computer engineering from Seoul National University, Seoul, South Korea, in 2013 and 2019, respectively. From 2019 to 2021, he was a Principal Research Engineer with Hyundai MOBIS, South Korea. Since 2021, he has been with the Gachon University, Seongnam, South Korea, where he is an Assistant Professor. His research interests include electric machine drives, electric/hybrid vehicles, and power electronic systems in various applications.

Seung-Ki Sul (S'78–M'87–SM'98–F'00) received the B.S., M.S., and Ph.D. degrees in electrical engineering from Seoul National University, Seoul, South Korea, in 1980, 1983, and 1986, respectively.

From 1986 to 1988, he was an Associate Researcher with the Department of Electrical and Computer Engineering, University of Wisconsin, Madison, WI, USA. From 1988 to 1990, he was a Principal Research Engineer with LG Industrial Systems Company, South Korea. Since 1991, he has been a member of faculty with the School of the Electrical and Computer Engineering, Seoul National University, where he is currently a Professor. He has authored or coauthored more than 150 IEEE journal papers and a total of more than 340 international conference papers in the area of power electronics. His current research interests include position sensorless control of electrical machines, electric/hybrid vehicles and ship drives, and power-converter circuits based on SiC MOSFET.

Dr. Sul was the Program Chair of IEEE Power Electronics Specialists Conference in 2006 and the General Chair of IEEE International Conference on Power Electronics and ECCE-Asia in 2011. From 2011 to 2014, he was the Editor-in Chief for the Journal of Power Electronics, which is an SCIE-registered journal, published by the Korean Institute of Power Electronics (KIPE), Seoul, South Korea. For year 2015, he was the President of KIPE. He was the recipient of the 2015 IEEE Transaction 1st and 2nd Paper Awards on Industrial Application, simultaneously. He was also the recipient of the 2016 Outstanding Achievement Award of the IEEE Industrial Application Society. He was also selected as the recipient of the 2017 Newell award sponsored by IEEE Power Electronics Society.